Table 1 Roughness function constants, $f(\eta_k) = a_i \ln \eta_k + b_i$

Zone	Ref. 2			Present data		
	η_k	a_i	b_i	η_k	a_i	b_i
Rough	$100 < \eta_k$	2.50	−3.00	$85 < \eta_k$	2.50	−3.85
Transition	$5.00 < \eta_k < 100$	2.84	−4.58	$12 < \eta_k < 85$	3.82	−9.45
Smooth	$\eta_k < 5$	0	0	$\eta_k < 12$	0	0

ment with the use of Eq. (2), but it must be pointed out that the Coles function normally would give better results if the measuring position were in the transition region between the laminar sublayer and fully turbulent portions of the boundary layer. It can be seen that the Preston-tube method can be considered accurate within ±6% for the test condition range of these data.

The series of tests[7] investigating the effects of grain-type surface roughness made use of the wind-tunnel diffuser floor surface plates, the skin-friction balance, and the total-pressure survey system, which were described in Ref. 1. These roughness data also were obtained at $M = 2.8$. Grain-type roughness was used in order that the results of these tests could be used to evaluate the extension of the Nikuradse roughness function[8] to the high Reynolds number compressible flow situation.

Three different grades of sand grain were tested. The mean diameters of the three grades, as determined by microscopic measurement, were 0.002, 0.004, and 0.010 in., respectively. The sand grains were bonded to the diffuser floor. The roughness covered the entire 4-ft width of the floor for a distance of 9 ft upstream of the instrumentation station. The skin-friction balance and total-pressure survey systems were installed side by side, offset equal distances from the tunnel longitudinal centerline.

As is the case with aerodynamically smooth surfaces, turbulent boundary layers over uniformly roughened surfaces exhibit certain velocity similarity characteristics. These characteristics are illustrated best by the defect law and law of the wall velocity profiles. The velocity defect law profiles of the present data indicated no effect of the surface roughness which was the expected result. Also, as expected, the law of the wall velocity profiles reflected the effect of the roughness. Figure 2 presents some profiles typical of the data obtained. It can be seen that, for the fully turbulent portion of the boundary layer over a surface with uniformly distributed roughness, the right-hand side of Eq. (1) can be expressed as $f(\eta) - f(\eta_k)$, where $f(\eta_k)$ is the so-called roughness function. In Ref. 8, Fenter correlated the roughness function as determined from the classical Nikuradse pipe flow experiments with the expression

$$f(\eta_k) = a_i \ln \eta_k + b_i \qquad \text{where} \qquad \eta_k = \rho_w U_\tau k/\mu_w \quad (3)$$

Figure 3 presents a comparison of the values of the roughness functions of the present data as obtained from the law of the wall profiles with the correlation of Ref 8. Table 1 presents the values of the a_i and b_i coefficients of Eq. (3) from Ref. 8 and from the present data. It is noted that the present data indicate that a higher degree of roughness can be permitted and still maintain an aerodynamically smooth surface, i.e., $f(\eta_k) = 0$. The velocity profile data and skin-friction measurements show the expected trends; however, the roughness function determined from the data is not in agreement with the roughness function as previously determined in incompressible pipe flow. This difference presumably is caused by a compressibility effect; however, other compressible data exist at lower Reynolds numbers that show reasonable agreement with the incompressible roughness function. Since tests were made at only one Mach number, further investigations to obtain additional data at other Mach numbers are considered necessary in order to resolve this problem.

References

[1] Moore, D. R. and Harkness, J., "Experimental investigations of the compressible turbulent boundary layer at very high Reynolds numbers," AIAA J. **3**, 631–638 (1965)

[2] Preston, J. H., "The determination of turbulent skin friction by means of surface pitot tubes," J. Roy. Aeron. Soc. **58** (February 1954).

[3] Hsu, E. Y., "The measurement of local turbulent skin friction by means of surface pitot tubes," David Taylor Model Basin Rept. 957 (August 1955).

[4] Fenter, F. W. and Stalmach, C. J., Jr., "The measurement of turbulent-boundary-layer shear stress by means of a surface impact pressure probe," J. Aerospace Sci. **25**, 793–794 (1958).

[5] Thompson, M. J. and Naleid, J. F., "Pressure gradient effects on the Preston tube in supersonic flow," J. Aerospace Sci. **28**, 940–944 (1961).

[6] Coles, D., "Measurements in the boundary layer on a smooth plate in supersonic flow," Ph.D. Thesis, California Institute of Technology, Pasadena, Calif. (1953).

[7] Moore, D. R. and Harkness, J., "Drag effects of surface roughness at high Reynolds numbers, $M = 2.8$," Ling-Temco-Vought Research Center Rept. 0-71000/4R-16 (June 1964).

[8] Fenter, F. W., "The turbulent boundary layer on uniformly rough surfaces at supersonic speeds," Vought Research Center Rept RE-E9R-2, Chance Vought Aircraft, Inc., Dallas, Texas (December 1959).

Very-Large-Deflection Behavior of Corrugated Strips

David L. Platus* and Shoichi Uchiyama*
Aerospace Research Associates Inc., West Covina, Calif.

Introduction

Few techniques have been developed for analyzing the very-large-deflection behavior of thin plate and shell structures, except for some very simple cases. Barton[1] and Bisshopp and Drucker[2] have obtained results for a cantilever beam subjected to a concentrated end load, based on the Bernoulli-Euler equation. Rhode[3] obtained similar results for the case of a uniformly distributed load.

In the present note, a technique is described† for handling the very-large-deflection behavior of a corrugated strip in terms of the solution to a curved cantilever beam with an end load (Fig. 1). A stepwise incremental solution is obtained for a modified Bernoulli-Euler equation, which permits both elastic and plastic deformation of beams of arbitrary shape. The technique involves incremental loads as well as incremental elements of the structure. For each incremental load application, the corresponding deformation of the curved

Received February 1, 1965; revision received May 20, 1965. This research was sponsored by the U. S. Air Force Office of Scientific Research under Contract No. AF 49(638)-1144. The authors wish to express their appreciation to Patrick J. Cunningham for obtaining the experimental results.

* Project Scientist.

† A more complete discussion is given in Refs. 4 and 5.

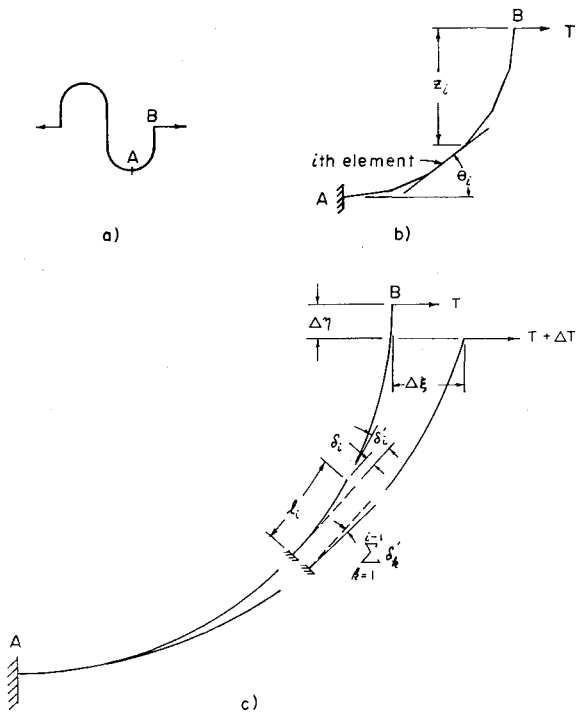

Fig. 1 Parameters used in incremental method.

cantilever beam is determined by accumulating rotations and deflections of short straight cantilever beams, which approximate the structure. Each incremental cantilever beam is subjected to a linearly varying moment and, in the plastic-range, linearly varying flexural rigidity. Results of the method are compared with a closed-form elastic solution and with experimental results.

Incremental Technique

The modified Bernoulli-Euler equation can be expressed by

$$-d\Delta\theta/ds = Tz/D' \tag{1}$$

where $\Delta\theta$ is the change in slope from the initial undeformed shape, s is the coordinate of length along the beam, T is the load per unit length of strip, z is the moment arm, and D' is an effective flexural rigidity. In the elastic range, D' has its usual definition and is constant; in the plastic range, it is defined as the ratio of moment to change in curvature and can be determined analytically or experimentally. Application of an incremental load ΔT results in a change in moment arm z as well as a change in D' where the structure is plastically deformed. The change in the right side of Eq. (1) due to ΔT can be expressed by

$$\Delta(Tz/D') = [z\Delta T + T\Delta z - (Tz/D')\Delta D']/D' \equiv \Delta M'/D' \tag{2}$$

where $\Delta M'$ represents the incremental moment as well as the incremental change in flexural rigidity. By selecting a moving set of Cartesian coordinates (x, y), with x tangent to the beam, the incremental change in the left side of Eq. (1) can be approximated by

$$-\Delta(d\Delta\theta/ds) = d^2\Delta y/dx^2 \tag{3}$$

where Δy is the incremental deflection normal to the beam. Equations (2) and (3) then yield

$$d^2\Delta y/dx^2 = \Delta M'/D' \tag{4}$$

which is applicable only for small values of x about the origin.

Equation (4) can be solved for each incremental cantilever beam, as illustrated in Fig. 1, by assuming linear variations in $\Delta M'$ and D'. Taking $x = 0$ at the base, the resulting incremental end slope δ_i' and end deflection δ_i for the ith beam are given by

$$\left.\begin{aligned}\delta_i' &\equiv d\Delta y/dx|_{x=l_i} = (\overline{\Delta M_{i-1}'} l_i/\overline{D_{i-1}'})[(1/\beta_i)(1 + \alpha_i/\beta_i)\ln(1+\beta_i) - \alpha_i/\beta_i] \\ \delta_i &\equiv \Delta y|_{x=l_i} = (\overline{\Delta M_{i-1}'} l_i^2/\overline{D_{i-1}'})\{(1/\beta_i)(1+\alpha_i/\beta_i)\times [(1/\beta_i)(1+\beta_i)\ln(1+\beta_i) - 1] - \alpha_i/2\beta_i\}\end{aligned}\right\} \tag{5}$$

where

$$\left.\begin{aligned}\alpha_i &\equiv (\overline{\Delta M_{i-1}'} - \overline{\Delta M_i'})/\overline{\Delta M_{i-1}'} \\ \beta_i &\equiv (\overline{D_i'} - \overline{D_{i-1}'})/\overline{D_{i-1}'}\end{aligned}\right\} \tag{6}$$

Here a subscript i on M' or D' denotes a quantity evaluated at the end of the ith element, and a bar denotes an average value during application of the load increment.

The horizontal and vertical incremental deflections of the end of the ith element relative to the $(i-1)$ th element are given by

$$\left.\begin{aligned}\Delta\xi_i - \Delta\xi_{i-1} &= \left(\delta_i + l_i\sum_{k=1}^{i-1}\delta_k'\right)\sin\left(\theta_i - \frac{1}{2}\sum_{k=1}^{i-1}\delta_k'\right) \\ \Delta\eta_i - \Delta\eta_{i-1} &= \left(\delta_i + l_i\sum_{k=1}^{i-1}\delta_k'\right)\cos\left(\theta_i - \frac{1}{2}\sum_{k=1}^{i-1}\delta_k'\right)\end{aligned}\right\} \tag{7}$$

where the summation term represents the rigid body rotation produced by the bending of all preceding elements. With the results of Eqs. (7), the incremental deflections can be accumulated from the base of the original cantilever beam in order to describe the complete deformation for each load increment. The computational procedure is as follows:

1) Initial values of z_i and θ_i are determined as indicated in Fig. 1b.

2) The first load increment ΔT is applied and the corresponding deflections are determined from classical small-deflection elastic theory.

3) With the results of step 2, the deflections are recomputed from Eqs. (2 and 5–7). The quantities $\overline{\Delta M_i'}$ are computed from Eq. (2) using $\overline{T} = \Delta T/2$, and similarly averaging the values of z_i. The values $\overline{D_i'}$ represent averages based on the resulting moments Tz_i before and after application of ΔT.

4) The values Δz_i are computed from the results of step 3 and compared with those of step 2. If the agreement is un-

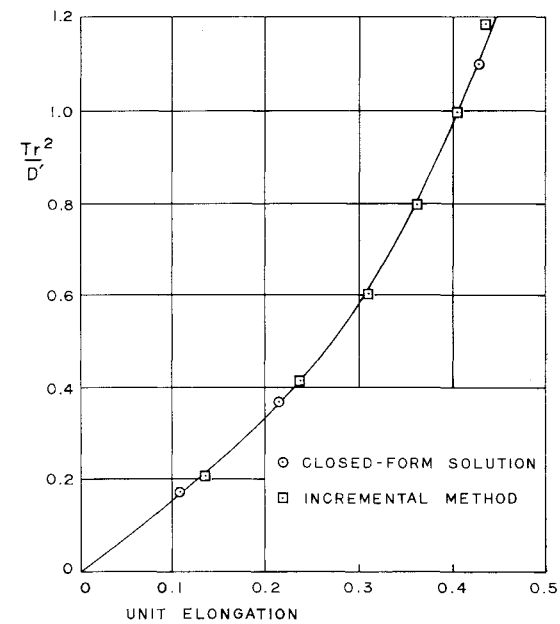

Fig. 2 Elastic load-deflection curve for semicircular-arc strip.

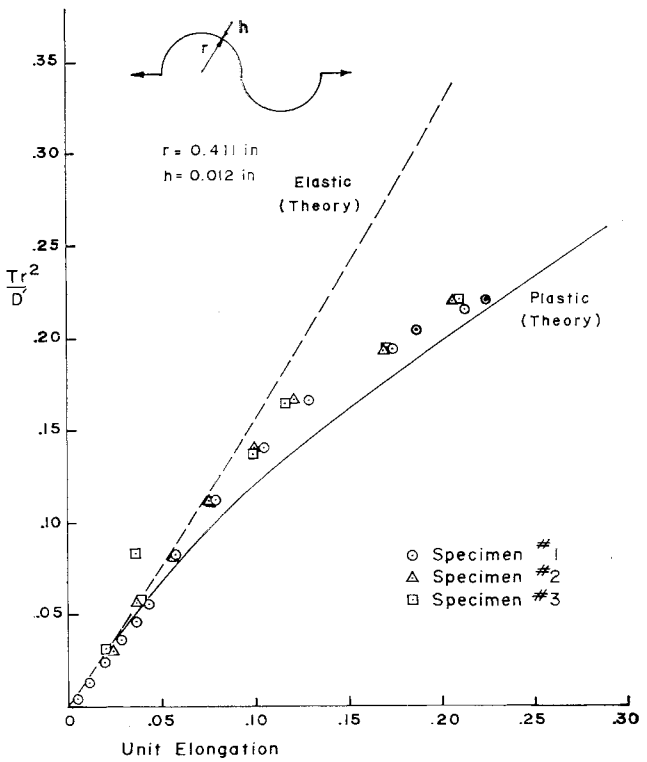

Fig. 3 Elastic-plastic load-deflection curve for semicircular-arc strip.

satisfactory, step 3 is repeated using, each time, the newly computed values for z_i, until agreement between two successive values is attained.

5) Subsequent load increments are applied following the procedure of steps 3 and 4, but load and deflection increments are accumulated in calculating T and z_i.

Closed-Form Elastic Solution

A closed-form elastic solution can be obtained for the case of a semicircular-arc strip of initial radius r and constant flexural rigidity. Differentiation of Eq. (1), with the change of variable $\varphi = \pi/2 - \theta$, yields

$$d^2\varphi/ds^2 = -(T/D')\cos\varphi \tag{8}$$

Boundary conditions are

$$\varphi(0) = \pi/2 \qquad \varphi(l) = \varphi_l \qquad (d\varphi/ds)(l) = 1/r \tag{9}$$

where $l = \pi r/2$. Multiplication of Eq. (8) by $d\varphi$, and integration from φ to φ_l with Eqs. (9), yields

$$\tfrac{1}{2}(d\varphi/ds)^2 = \lambda^2(\sin\varphi_l - \sin\varphi) + 1/(2r^2) \tag{10}$$

where $\lambda^2 \equiv T/D'$. With this result, the deflections can be written

$$\left.\begin{aligned}\xi &= \int_0^l \sin\varphi\, ds - r = -\\ &\qquad \frac{1}{2^{1/2}\lambda}\int_{\pi/2}^{\varphi_l} \frac{\sin\varphi}{(\sin\varphi_l - \sin\varphi + \zeta^2)^{1/2}}\, d\varphi - r\\ \eta &= r - \int_0^l \cos\varphi\, ds = r +\\ &\qquad \frac{1}{2^{1/2}\lambda}\int_{\pi/2}^{\varphi_l} \frac{\cos\varphi}{(\sin\varphi_l - \sin\varphi + \zeta^2)^{1/2}}\, d\varphi\end{aligned}\right\} \tag{11}$$

where $\zeta^2 \equiv 1/(2\lambda^2 r^2)$. With the further changes of variable,

$$\left.\begin{aligned}1 + \sin\varphi &\equiv 2\sin^2\psi\\ \psi_l &\equiv \sin^{-1}(1/K^2 - \zeta^2/2)^{1/2}\\ 1 + \sin\varphi_l + \zeta^2 &\equiv 2/K^2\end{aligned}\right\} \tag{12}$$

Table 1

No. of increments	ξ/r Tr^2/D'	η/r Tr^2/D'	% error in ξ	% error in η
3	0.757	0.505	−3.6	1.0
4	0.770	0.504	−1.9	0.8
5	0.775	0.501	−1.3	0.2

Eqs. (11) become

$$\left.\begin{aligned}\frac{\xi}{r} &= -\frac{K}{\lambda r}\int_{\pi/2}^{\psi_l} \frac{(2\sin^2\psi - 1)\, d\psi}{(1 - K^2\sin^2\psi)^{1/2}} - 1\\ \frac{\eta}{r} &= 1 + \frac{2K}{\lambda r}\int_{\pi/2}^{\psi_l} \frac{\sin\psi d(\sin\psi)}{(1 - K^2\sin^2\psi)^{1/2}}\end{aligned}\right\} \tag{13}$$

which can be solved to give the desired results

$$\left.\begin{aligned}\xi/r = {} & 2^{1/2}\zeta(2/K - K)[F(K, \pi/2) - F(K, \psi_l)] -\\ & 2(2)^{1/2}(\zeta/K)[E(K, \pi/2) - E(K, \psi_l)]\\ \eta/r = {} & 1 - 2(\zeta/K)[K\zeta - 2^{1/2}(1 - K^2)^{1/2}]\end{aligned}\right\} \tag{14}$$

where $F(K, \psi)$ and $E(K, \psi)$ are the elliptic integrals of the first and second kind, respectively.

Numerical Examples

A numerical example was carried out for a semicircular-arc strip loaded in the elastic range. The incremental elastic solution is shown in Fig. 2, compared with the closed-form result of Eqs. (12) and (14). The cantilever beam of Fig. 1 was divided into four increments of length, and six load increments were used, as indicated by the square points in Fig. 2. The computations were carried out on a desk calculator.

The incremental technique was also used to predict the elastic-plastic behavior of a semicircular-arc stainless-steel strip, and the results were compared with experiment, as shown in Fig. 3. The moment-curvature or D' values used in the calculations were determined experimentally from bend tests on flat specimens of the same sheet metal used to form the corrugated strips. As in the elastic case, four length increments and six load increments were used to compute the curve of Fig. 3.

The incremental beam approach gives surprisingly good results for relatively few increments. This is further illustrated in Table 1 which gives the errors in the small-deflection elastic solution for the semicircular-arc configuration, computed on the basis of three-, four-, and five-length increments.

Conclusions

The present incremental technique represents a simple and powerful tool for handling the very-large-deflection elastic-plastic behavior of corrugated strips of arbitrary shape. The use of an effective flexural rigidity permits variation in thickness as well as plastic behavior, and the treatment of a cantilever beam with end load can readily be extended to other forms of loading. Sufficiently few increments of load and length are required, so that the method is suitable for use with a desk calculator.

References

[1] Barton, H. J., "On the deflection of a cantilever beam," Quart. Appl. Math. **2**, 168–171 (1944).

[2] Bisshopp, K. E. and Drucker, D. C., "Large deflection of cantilever beams," Quart. Appl. Math. **3**, 272–275 (1945).

[3] Rhode, F. V., "Large deflections of a cantilever beam with uniformly distributed load," Quart. Appl. Math. **11**, 337–338 (1953).

[4] Platus, D. L., Cunningham, P. J., Marovich, F. A., and Mazelsky, B., "Research on energy absorbing structures, Part 1—Final report," Air Force Office of Scientific Research Contract AF 49(638)-1144, ARA, Inc. (February 1963).

[5] Platus, D. L., Vchiyama, S., Cunningham, P. J., Marovich, F. A., and Freeman, H, H., "Research on energy absorbing structures, Part II—Final report," Air Force Office of Scientific Research Final Scientific Rept. 64-0154, Contract AF 49(638)-1144, ARA, Inc. (February 1964).

Effect of Ablation on Momentum Deposition in the Wake of a Re-Entry Vehicle

A. G. Hammitt*
TRW Space Technology Laboratories, Redondo Beach, Calif.

THE wake of an unpropelled vehicle is distinguished by a velocity and energy difference from the ambient condition. The vehicle loses momentum and energy, which are deposited in the wake behind it. For a slender, pointed re-entry vehicle, the momentum and energy loss from the vehicle caused by the pressure drag are spread out from the vehicle by the shock wave so that the changes in the energy and momentum of the affected flow are small, but the friction force causes a large change resulting in the part of the wake which is detectable.

For an ablating vehicle, the momentum deposited in the wake and the drag on the vehicle are not the same since the mass of the vehicle is changing. The momentum input to the wake is not the same for an ablating as for a non-ablating vehicle and is not equal to the drag on the vehicle if ablation is taking place. The purpose of this note is to explore this effect and determine the magnitude of the momentum loss associated with the ablation. The effect will be compared only with the friction drag, since this is the important drag for determining the wake of a sharp body, which is the case in which this phenomenon is of greatest interest.

The total loss of momentum of the vehicle I is the friction force F plus the momentum associated with the ablated mass $\dot{m}$:

$$I = F + \dot{m}V \tag{1}$$

The total mass loss by ablation is

$$\dot{m} = q/L = \tfrac{1}{2}\rho\, V^3 A C_H/gJL \tag{2}$$

where L is the heat of ablation of the material. The skin friction $F = \frac{1}{2}\,\rho V^2 A C_f$. Therefore,

$$I = \tfrac{1}{2}\,\rho A V^2 C_f\,[1 + (V^2 C_H/gJL\,C_f)] \tag{3}$$

Equation (3) shows that the actual skin-friction term is augmented by an ablation term, which depends on the ratio of freestream kinetic energy to the heat of ablation of the material and the ratio of heat transfer to friction coefficients.

Since the skin friction is affected by the rate of ablation, the preceding expression does not allow a comparison with the nonablation skin friction. To obtain this comparison, boundary-layer solutions, with fluid injection, must be considered. Because laminar flow over a cone lends itself to analytic treatment, with appropriate simplifying assumptions, this case will be used to demonstrate the important physical phenomena and the size of the effect. If the usual simplification of $Pr = Le = 1$ and $\rho\mu$ const are made, then the modified skin-friction parameter becomes a unique function of the modified blowing parameter similar to the incompressible case (Fig. 1).[1,2] By combining Reynolds analogy ($C_H = \frac{1}{2}C_f$, which follows from the assumptions already made) with Eq. (2), a relation between the blowing rate and skin friction based on the ablation properties can be found if all of the ablation products are considered to be emitted as gas:

$$\frac{(2\dot{m}/\rho VA)\,(Re_\infty/C)^{1/2}}{C_f(Re_\infty/C)^{1/2}} = \frac{V^2}{2gJL} \tag{4}$$

The relation is also plotted on Fig. 1 for different values of $V^2/2gJL$. The intersections of the curves are the solutions for C_f and $\dot{m}$. Equation (3) can now be written in terms of C_{f0}, the value of skin friction for a nonablating surface. This relation is plotted in Fig. 2. Typical values of L are between 1000 and 10,000 Btu/lb, so that at velocities of the order of 20,000 fps, $V^2/2gJL$ is between values like 1 and 10.

Although the simplified theory used here to describe the laminar boundary layer with injection is not precise, it does give a useful demonstration of the size of the effect being considered without obscuring the physical phenomena with involved numerical details. For a real case, appropriate values of Pr and Le should be used based on actual ablation products.

It may be concluded that the actual momentum deposited in the wake by the viscous effect of an ablative vehicle is larger than the nonablating vehicle. For laminar flow on a cone, it does not exceed approximately twice the nonablative vehicle value for the simplified case considered.

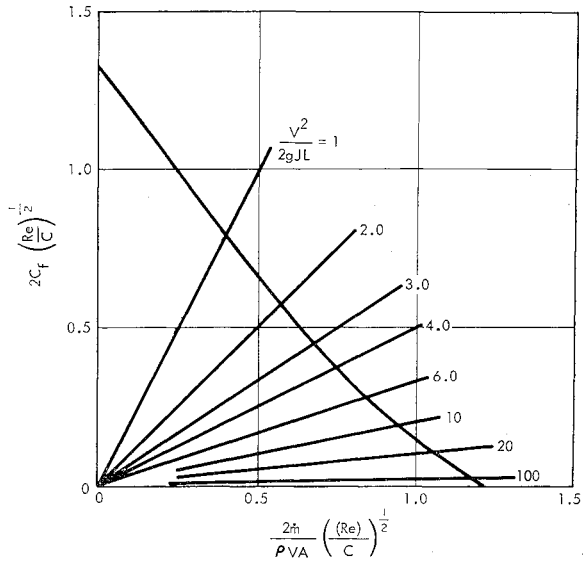

Fig. 1 Relation between skin friction and blowing rate.

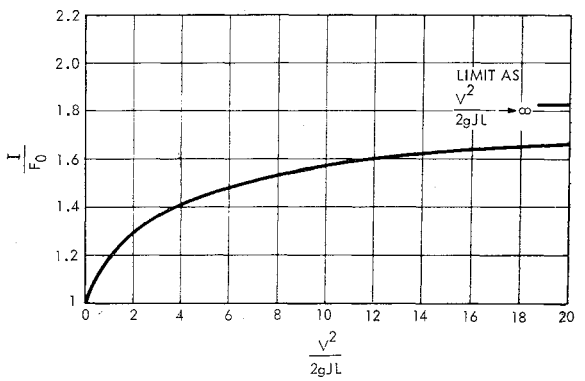

Fig. 2 Momentum deposition compared with zero ablation skin friction for different values of kinetic energy heat of ablation ratio.

Received March 15, 1965; revision received April 29, 1965.
* Manager, Aerophysics Department. Member AIAA.